Surface & Coatings Technology 452 (2023) 129133

Contents lists available at ScienceDirect

Surface & Coatings Technology

journal homepage: www.elsevier.com/locate/surfcoat

RSM models approach for optimization of the mechanical properties of electroless Ni-B-nanodiamond coating: An experimental and molecular dynamic simulation study

Sepehr Yazdani *, Veronique Vitry

Metallurgy Department, Faculty of Engineering, University of Mons, 20, Place du Parc, Mons, Belgium

ARTICLE INFO

Keywords:
Composite coating
Molecular dynamics simulations
Nanodiamonds
Scratch resistance
Electroless Ni-B
Raman spectra

ABSTRACT

This report explores the effects of electroless Ni-B-nanodiamond plating bath parameters for optimization of the hardness and deposition rate based on response surface method (RSM). Quadratic models were developed and found to be mathematically appropriate for the optimization. The nanodiamonds (ND) and optimized coating were characterized using XPS, DLS, FIB-SEM, GDOES, microhardness, and nanoindentation. The results of the molecular dynamic simulation show low adsorption energy of borohydride on nanodiamonds surface is not favourable for borohydride dehydrogenation, therefore the boron content of the coating decreases when ND are added. Raman spectroscopy, SEM, and EDS analysis carried out on different zones of the surface after scratch test show nanodiamonds undergo graphitization and micro-cracking which block crack propagation at lower load. In addition, ND improves formation of the tribolayer at higher loads. The Raman spectroscopy results after indentation tests show the possibility of SP3 to SP2 phase transformation for nanodiamonds. The molecular dynamic simulation results confirm that phase transformation through monitoring the changes in nanodiamonds interatomic potential and interatomic distances. It is believed that the volume expansion caused by this phase transformation increases the toughness of coating.

1. Introduction

Electroless Ni—B plating is based on the oxidation and reduction reactions, using a strong reducing agent such as sodium borohydride to form a dense coating on the surface of various materials [1–3]. The substrates that are used for the plating can itself be catalytic or can be activated by the use of displacement deposits [4]. Among all of the used substrates mild steels have strong catalytic activity and needs no activation process prior to deposition [1]. However, sensitization such as using $PdCl_2$ or SnCl has been reported for stainless steel, copper, polymer, and ceramics substrates to improve the deposition rate [1,5].

Ni—B coatings have been widely used in automobile, chemical, and aerospace industries that needs hard material for various mechanical applications [6–8]. Their crystal structure directly after plating (as-plated coating) is semi-crystalline [9] while a fully crystalline structure is obtained after heat treatment between 300 and 600 °C [10]. The heat-treated coatings have higher hardness but they are more susceptible to crack formation when loads are applied on them due to their brittle crystal structure [11–13]. For this reason, new researches are inclined towards improving the mechanical properties of the as-plated electroless Ni—B coatings.

The addition of nanoparticles to synthesize composite coating is a well-known method for improving the mechanical properties of as-plated coatings [14–17]. Among the reinforcement particles, nanodiamonds (ND) have highest hardness, young's modulus, and low friction coefficient, which makes them great candidates to be used in composites [18,19]. Nanodiamonds are usually made of sp3 carbon core and sp2 carbon shell [20,21]. The SP3-hybridized carbon is known for its hardness and wear resistance, whereas sp2-hybridized carbon is associated with lubricity and friction reduction [22,23]. Crack pinning, crack deflection, high tensile strength, and high elastic modulus have been reported as the main reinforcement mechanisms of nanodiamonds in composites [24–26].

In the study of the electroless Ni-B-nanodiamond it has been reported that nanodiamond particles act as barriers against plastic deformation and ND increase the coating hardness from 590 to 700 $HV_{0.1}$ [27]. Makarova et al. on the study of the wear resistance of the nickel-nanodiamond composite coating showed that the ND improves

---

* Corresponding author.
E-mail address: Sepehr.yazdani@umons.ac.be (S. Yazdani).

https://doi.org/10.1016/j.surfcoat.2022.129133
Received 19 October 2022; Received in revised form 21 November 2022; Accepted 2 December 2022

adhesive wear resistance of the coating by increasing the hardness [28]. Beside, nanodiamond particles also play an important role as lubricating agents, helping to weaken the abrasion of composite coating [29]. In the case of crystalline composite coating nanodiamonds impede the grain growth and dislocation movement which results in low plastic deformation [30–32].

Although some work has already been reported on nanodiamond composite coating, most of them rely on hardness improvement, grain refinement, and nanodiamonds lubricating effect to explain the role of nanodiamonds on improvement of coating adhesion. There is limited research concerning evaluation of the nanodiamonds atomic structure after adhesion and toughness tests on composite coating. In this case, the use of Raman spectroscopy to obtain ND vibrational and crystallographic information and of molecular dynamic simulation helps gaining better understanding of the improvement mechanisms.

On the other hand, dispersion of the nanoparticles in the electroless bath is affected by various parameters. Among those, surface chemistry of the particles [33] and bath plating composition [34] changes more significantly the driving force for nanoparticles deposition [35–37]. Therefore, optimization of these parameters is needed to achieve adequate interfacial bonding and inhibit de-attachment of particles.

The purpose of this work is to address the aforementioned problems by first optimizing bath plating parameters of electroless an Ni-B-nanodiamond plating process aiming towards improvement of coating hardness and plating rate using response surface method (RSM). Afterwards, the role of the nanodiamonds in the bath reaction, chemical composition, scratch resistance and toughness of the Ni—B coating will be investigated through in-depth analysis of nanodiamonds atomic structure using Raman spectroscopy and molecular dynamic simulation.

2. Materials and methods

2.1. Substrate preparation

The ST 37 mild steel, with a size of 50 × 25 × 1 mm^3 was used as a substrate. The substrates were ground with SiC paper up to 800 grits. After grinding, the substrates were degreased with acetone for 3 min and rinsed with distilled water. Finally, samples were immersed in 30 vol% HCl acid for 1 min for activation and directly transferred to the plating bath.

2.2. Functionalization of the nanodiamonds

Nanodiamonds (95 % purity) were purchased from Sigma Aldrich. The powders were immersed in HNO_3/H_2SO_4 (1:3 V/V) solution for 1 h under ultrasonic agitation. The functionalized powders were filtered and rinsed with distilled water then dried at 100 °C.

2.3. Statistical design of experiment

The RSM method was applied to design the experiments and determine optimal deposition conditions to attain the maximal deposition rate and hardness for electroless Ni-B-nanodiamond coating. The influence of 3 crucial variables: nanodiamond, reducing agent, and stabilizer concentration (Table 1) on coatings hardness and deposition rate was evaluated. The concentration of other bath components including nickel chloride hexahydrate as nickel source (24 g/l), ethylenediamine as complexing agent (60 g/l), and Cetrimonium bromide (CTAB) surfactant (0.72 g/l) were kept constant for all the experiments. Plating was carried out at 95 ± 1 °C for 60 min under magnetic stirring, and the pH value was adjusted at 14 by addition of NaOH (40 g/l).

Table 1
Variables and range of variation for RSM experimental design of electroless nickel-boron plating bath containing nanodiamonds.

Variables	Range of variables (g/l)	
	Minimum	Maximum
Nanodiamond concentration	0.1	0.5
Reducing agent concentration ($NaBH_4$)	0.6	1.8
Stabilizer concentration ($SnCl_2$)	0.02	0.1

A central composite design (CCD) with a total number of 15 experiments was chosen to determine experimental points. The relationship between the three variables and responses (hardness and thickness) are estimated using Design Expert Software and the arrangement of all the design point combinations and their corresponding experimental response values obtained are shown in Table 2.

It should be noted that each of the fifteen experiments for fabrication of the coating has been repeated at least two times just to limit experimental errors by comparing the average thickness and microhardness value. After being sure about reproducibility of process, the obtained data from one of these two identical samples were reported.

2.4. Measurement of coatings responses

Microhardness and thickness of the coatings were measured on mounted and polished cross-sections of the samples. Microhardness measurements were performed with a hardness tester using Knoop micro-indentation on the cross section of samples, with a load of 50 g and holding time of 20 s according to ASTM E384 standard. The thickness of the samples was measured using a HIROX KH-8700 (Tokyo, Japan) digital optical microscope with 3000× magnification and 101.1 μm horizontal field of view. For both tests the average value of the 20 measurements on the coatings were reported.

2.5. Characterization of nanodiamonds and optimized coating

The bonding structure of the nanodiamonds before and after the functionalizing process were analysed using an ESCA-5000 Versa Probe X-ray photoelectron spectroscopy system with the following X-ray settings: beam size diameter: 200 μm; beam power: 50 W; voltage: 15 kV. The pressure in the analysis chamber was 2 × 10–6 Pa. The XPS data were collected using monochromatic AlKα radiation at 1486.6 eV and photoelectrons were collected at a take-off angle of 45° to the surface normal.

The size distribution of the nanodiamonds were measured by dynamic light scattering (DLS) at 25 °C and a scattering angle of 173° in auto mode. 1 mL dilute dispersion of each solution with the concentration of 0.2 wt% nanodiamonds filled in the quartz cuvette was used for measurement immediately after sonication.

Scanning electron microscopy (SEM) coupled with Energy Dispersive Spectrometry (EDS) was used to study the surface morphology and scratched surface of the coatings.

The chemical composition profile of the coating was investigated by GD-OES (Glow Discharge-Optical Emissions Spectroscopy).

A dual beam microscope (Focused Ion Beam-Scanning Electron Microscopy, FIB-SEM) was used to observe the cross section texture of the coatings.

Nanoindentation was carried out on polished coating cross section, and the maximum penetration depth of the indenter was 300 nm. The results are the average value of 20 measurements. The load–displacement curves were analysed by the Oliver and Pharr method.

Scratch tests with continuous load method using diamond Rockwell stylus with a radius of 200 μm was used according to ASTM C1624 standard on the coating surface. The tests were performed on the coatings surface with a load rate of 100 N.min-1 and an advance rate of 6.75 $mm.min^{-1}$. The final load of the test was 150 N, resulting in a scratch distance of 10 mm.

Raman spectroscopy was used on the different parts of the scratched surface of the coatings. The power was set at 100 mW and the spectrum was recorded in the 800 to 2000 cm^{-1} range using a micro-Raman system spectrometer. Measurements were carried out 4 times on each

Table 2
Experimental parameters of CCD design for optimization of electroless nickel-boron bath containing nanodiamonds, and corresponding responses.

Number (n)	ND concentration (g/l)	Reducing agent concentration (g/l)	Stabilizer concentration (g/l)	Thickness (μm)	Microhardness (hk_{50})
1	0.3	1.2	0.06	12.0 ± 0.9	871 ± 36
2	0.3	1.2	0.10	12.5 ± 0.9	780 ± 27
3	0.3	1.8	0.06	14.0 ± 1.1	820 ± 32
4	0.3	1.2	0.02	6.5 ± 0.5	690 ± 20
5	0.1	1.2	0.06	15.0 ± 1.0	730 ± 27
6	0.3	0.6	0.06	12.5 ± 0.3	750 ± 29
7	0.5	1.2	0.06	12.0 ± 0.8	820 ± 33
8	0.1	0.6	0.02	8.5 ± 0.8	630 ± 13
9	0.5	0.6	0.02	5.0 ± 0.4	650 ± 15
10	0.1	1.8	0.02	10.6 ± 0.2	550 ± 11
11	0.1	0.6	0.10	14.0 ± 0.9	608 ± 13
12	0.5	0.6	0.10	11.0 ± 0.8	580 ± 15
13	0.1	1.8	0.10	16.0 ± 0.8	730 ± 21
14	0.5	1.8	0.02	7.5 ± 0.6	580 ± 11
15	0.5	1.8	0.10	14.0 ± 1.1	730 ± 23

point.

The toughness of the coatings was studied qualitatively using the Rockwell C indentation test according to ASTM E18 standard. The cone-shaped diamond with a 120° angle at the tip (200 μm in radius) was pressed perpendicularly on the coating with a normal load of 150 kg, SEM and Raman spectroscopy were used to study the impact of indentation on the coatings surface.

2.6. *Molecular dynamic simulation*

Materials studio software was utilized for MD simulation and calculation of borohydride adsorption energy on Fe (substrate), Ni (coating matrix), nanodiamond (nanoparticles). The MD simulation will help to understand how nanodiamonds affect the reduction reaction during the deposition and modifies boron content of coating. Al crystalline surface (Fe, Ni, nanodiamond) with (100) plane (the plane with the most negative value of Gibbs energy) was constructed by cleaving its unit cell. The minimum surface thickness of 15 Å was set as a cleaved surface. Afterwards, a vacuum layer of at least 20 Å was added in the z-direction to eliminate the effects of periodic boundary conditions. The electrolyte was constructed by designing a mixture of 100 water molecules, and 10 Na^+ and BH_4^- ions. The charge of each anion and cations was assigned using the current method. The final solutions were placed over the defined surfaces through the layer builder module.

The cells were subjected to a 500 ps minimization process under Canonical Ensemble (NVT) condition for reaching equilibrium condition. The dynamics task of the Forcite module was applied to simulate the adsorption of the borohydride into the defined layers. The potential energy of simulation system was expressed using the Universal force field. The van der Waals and electrostatic non-bonded interactions were computed with the use of atom-based cutoff and Ewald methods, respectively. The velocity verle integration algorithm was applied to solve Newton's equation of motion with integration time steps of 1 fs (10^{-15} s). The operational temperature was monitored via Andersen thermostat [38].

To understand the effect of the indentation force on nanodiamonds SP2 and SP3 carbon structure, MD simulation using Lammps software was carried out. The simulation model which consists of a sp2 and sp3 carbon layer (separately) with a spherical indenter. The ratio of the SP3 to SP2 carbon was adjusted according to the XPS analysis. The Adaptive Intermolecular Reactive Empirical Bond Order potential (AIREBO) potential for hydrocarbons was defined as an interatomic potential [39]. The indenter tip with the radius of 60 Å was made of carbon atoms in the diamond cubic structure and remains rigid during the simulations.

One of the major limitations of the MD approach is that indenter velocity is considerably larger than the sliding velocities in the real tests [40]. Therefore, in this study, we did not intend to make a direct quantitative comparison between experimental and MD results; instead, the trends were considered. V = 100 m/s was chosen for the indenter velocity, and the change in the SP2 and SP3 interatomic potential and phase transformation was monitored.

3. Result and discussion

3.1. *Nanodiamonds characterization*

The XPS C1s high-resolution peaks of raw and acid treated nanodiamond powders are plotted in Fig. 1. The deconvolution and fitting consist of 5 binding energies at 284.5 eV (sp2), 285.3 eV (sp3), 286.3 eV (C—O), 287.6 eV (C=O), and 288.6 eV (–COOH) [41,42]. The deconvolution results have been tabulated in Table 3. The SP3 to SP2 ratio of nanodiamonds after the acid treatment decreases from 2.96 to 1.66, and C—O bonding presents higher intensity than C=O bonding after acid treatment.

It has been proved in previous publications that in acid treatment after breaking of C=C bonds [10], oxygen molecule is chemisorbed nearby, pull apart the carbon ring and produce a crown ether configuration in the SP2 carbon network [43,44]. This hypothesis can be verified in our results since the bonding energies related to sp2 hybridized carbon shifted −0.1 eV. In other words, after the oxygen molecules pull apart the carbon ring the electron density around the sp2 carbon element increases and the binding energy decreases. Therefore, binding energy peak shifts negatively.

Fig. 2 shows particle size distribution of 0.2 wt% pristine and acid treated ND solution. The hydrodynamic diameter for the acid treated nanodiamonds varies between 430 and 630 nm, however, the hydrodynamic diameter of the pristine nanodiamonds is between 900 and 1210 nm. Results clearly indicates that the functional groups at the nanodiamonds surface prevent their agglomeration. This is due to the fact the carboxylic group in acid treated nanodiamonds releases H^+ in alkaline solution and create repulsive force between the negatively charged nanodiamonds [45]. On the other hand, existence of more oxygen bonding groups on acid treated sample improves nanodiamonds basicity which increases its stability in basic solution [46]. The visual observation of the ND suspension stability is presented in Supporting Information (Fig. S1).

3.2. *Effect of deposition variables on hardness and thickness of Ni-B-nanodiamonds coatings*

An analysis of variance (ANOVA) was performed for the model fitting of the hardness and thickness data. Data fitting showed that the quadratic model was the most suitable model (Table. 4) for both responses. No significant difference ($p > 0.05$) was found between the experimental and predicted values.

The equation developed after the fitting process to determine the

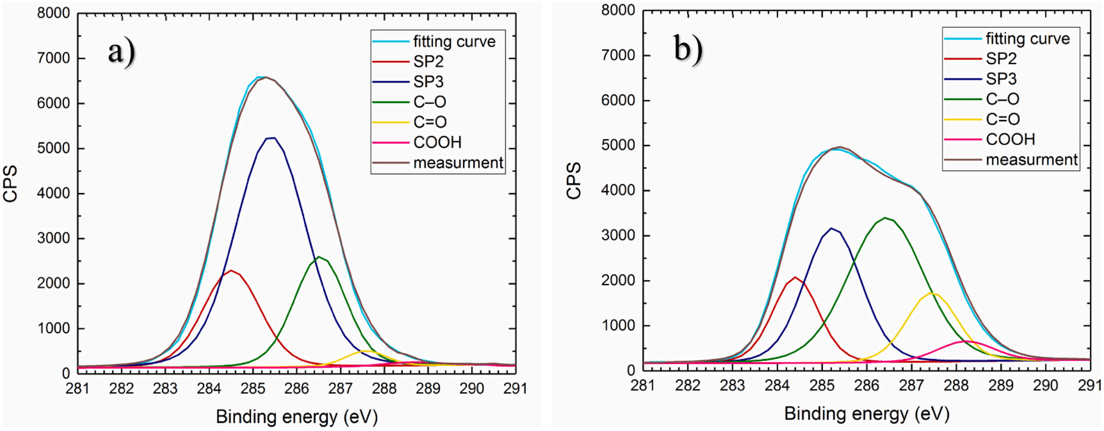

Fig. 1. Typical high-resolution XPS spectra in C 1s region of (a) raw and (b) acid treated nanodiamonds.

Table 3
XPS deconvolution results of C 1s peak for raw and acid treated nanodiamonds.

Component name	Peak position (eV)		FWHM (eV)		Concentration (at. %)	
Sample name	raw	Acid treated	raw	Acid treated	raw	Acid treated
SP2	284.51	284.40	1.5	1.2	19.5	15.43
SP3	285.40	285.23	1.9	1.5	57.81	26.18
C-O/C-N	286.53	286.42	1.39	1.9	20.27	40.81
C=O/N-C=O	287.58	287.45	1.2	1.3	2.17	13.41
COOH	288.54	288.21	1.5	1.4	0.25	4.17

thickness as responses to input variables A (nanodiamond concentration), B (reducing agent concentration) and C (stabilizer concentration) can be expressed as follows:

$$\text{Thickness} = 12.21 + 1.46 \times A + 1.1 \times B + 2.94 \times C + 0.175 \times AB + 0.2 \times AC + 0.05 \times BC + 0.9818 \times A^2 + 0.7318 \times B^2 - 3.02 \times C^2 \quad (1)$$

Fig. 3a shows that at every concentration of the nanodiamonds there is an almost direct relation between reducing agent concentration and coating thickness. Fig. 3b shows that stabilizer concentration has a profound effect on the coating thickness: increasing stabilizer concentration up to 0.06 g/l at every concentration of reducing agent, increases

Table 4
Fit summary of the proposed models for hardness and thickness of composite coatings.

Response	Suggested model	F Value	*P*-value	Statistical status
Thickness	Quadratic	128.79	<0.0001	Significant
Hardness	Quadratic	39.91	<0.0001	Significant

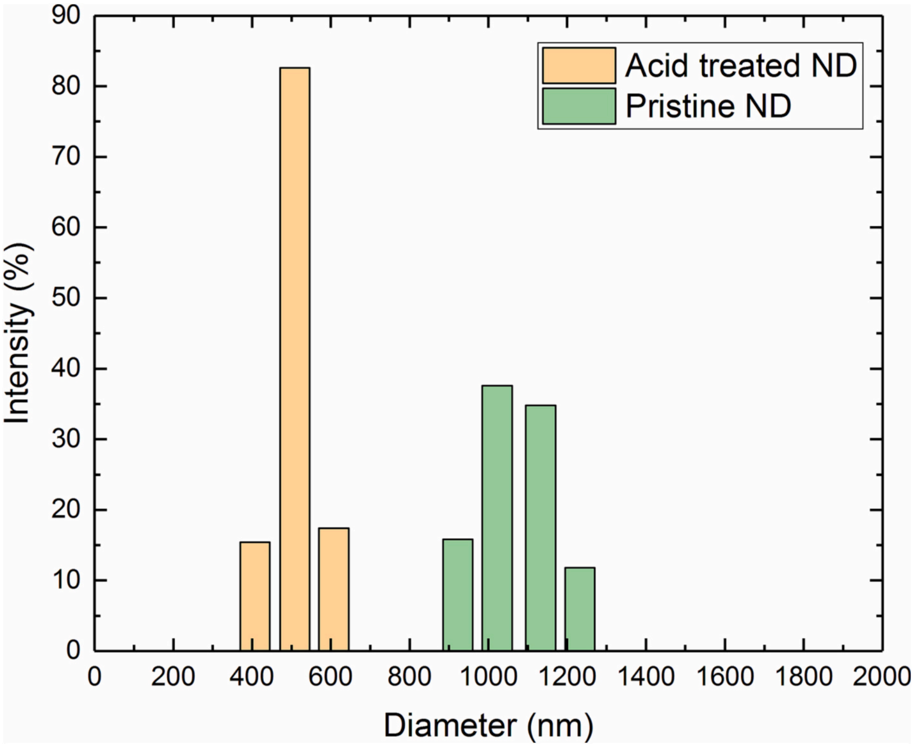

Fig. 2. DLS results of the 0.2 wt% pristine and acid treated ND alkaline solution (pH 14).

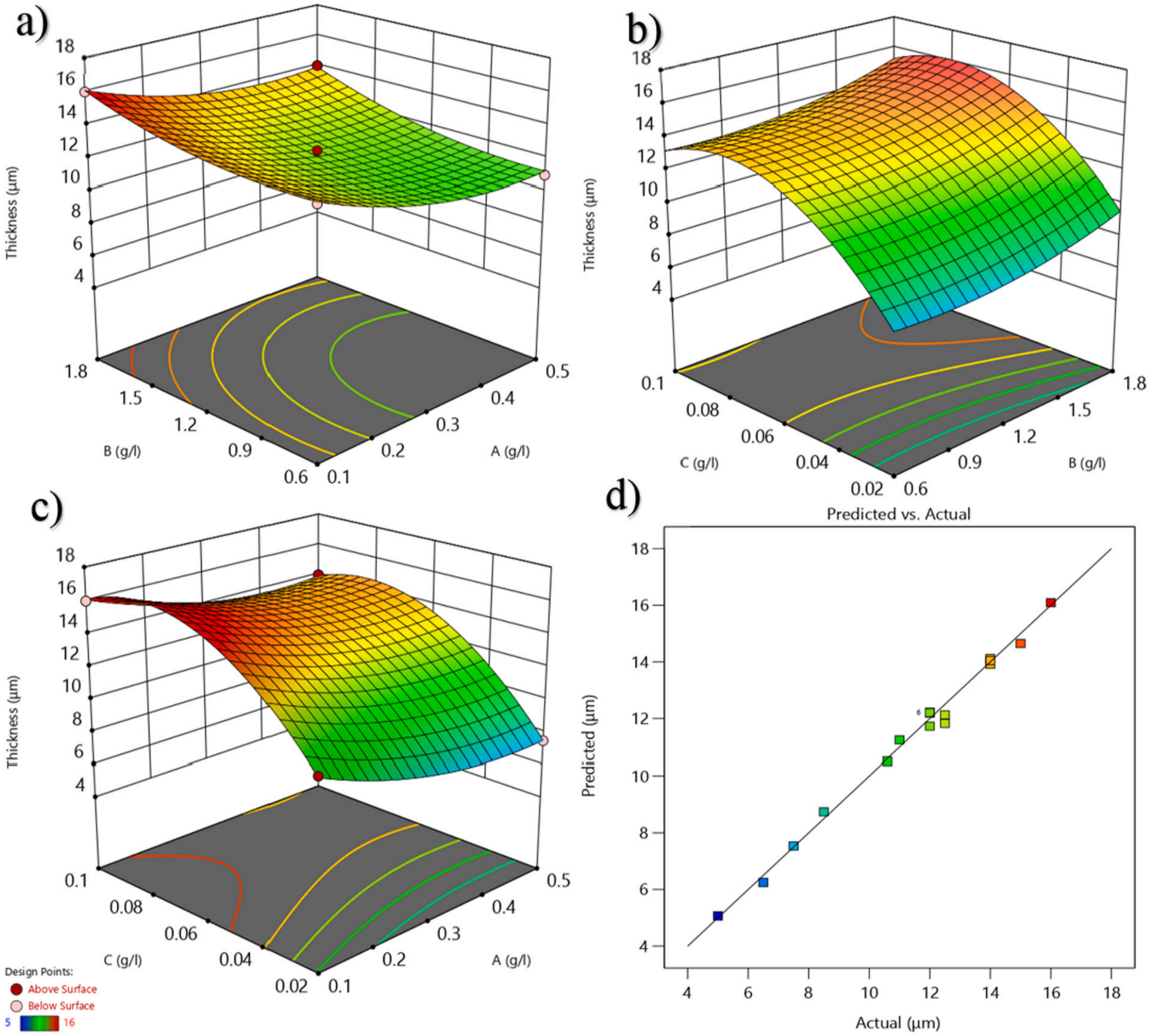

Fig. 3. 3D surface of the effect of a) A and B, b) B and C, c) A and C, variables on the thickness, and d) Plot of the experimental thickness values versus predicted values by RSM.

the coating thickness, and raising the concentration from 0.06 up to 0.1 g/l slightly decreases thickness.

Fig. 3c shows that at the stabilizer concentration of e 0.02 and 0.1 g/l the coating thickness does not change significantly when changing the nanodiamond concertation which indicates these concentrations as the lower and upper limits for the electroless bath stability.

Fig. 3d shows the normal probability plots of the residuals, the data distributed normally which demonstrate the high accuracy of the thickness model ($R^2 = 98.37$ %).

The equation of the developed model showing the hardness as response can be expressed as follows:

$$\text{Hardness} = 859.47\ 11.2 \times A + 19.2 \times B + 32.8 \times C + 4.75 \times AB - 9.75 \times AC + 52.75 \times BC - 67.18 \times A^2 - 57.18 \times B^2 - 107.18 \times C^2 \quad (2)$$

The response surface plots of the coatings hardness as a function of defined variables are shown in Fig. 4a-c. Results show that increasing the reducing agent concentration from 0.6 to 1.5 g/l at every concentration of nanodiamonds significantly increases the microhardness of the composite coatings, however, it is more pronounced at a concentration of nanodiamond of 0.3 g/l. Further increasing of the reducing agent concentration from 1.5 g/l to 1.8 g/l leads to lower microhardness value.

At the stabilizer concentrations of 0.02 and 0.10 g/l which have been described previously as the upper and lower stability limits of the electroless bath solution, the microhardness shows a low value which is in consistence with the results obtained for the thickness.

The R-squared statistic in the Fig. 4d indicates that the model explains 94.85 % of the variability of the response.

3.3. Bath parameter optimization for fabrication of Ni-B-nanodiamond coating

After the models for both responses were fitted, the maximum coating microhardness and thickness value was set as the goal of the optimization process. The RSM optimization results for variables and the predicted responses are tabulated in Table 5.

The optimized Ni-B-nanodiamond coating was fabricated according to the optimum conditions obtained from Table. 5. The effect of nanodiamonds on microstructure, chemical composition, scratch resistance, and toughness of the coating has been assessed by comparing the optimized Ni-B-nanodiamond coating with a coating obtained in exactly the same deposition conditions without nanodiamonds (Ni—B coating) in the following sections.

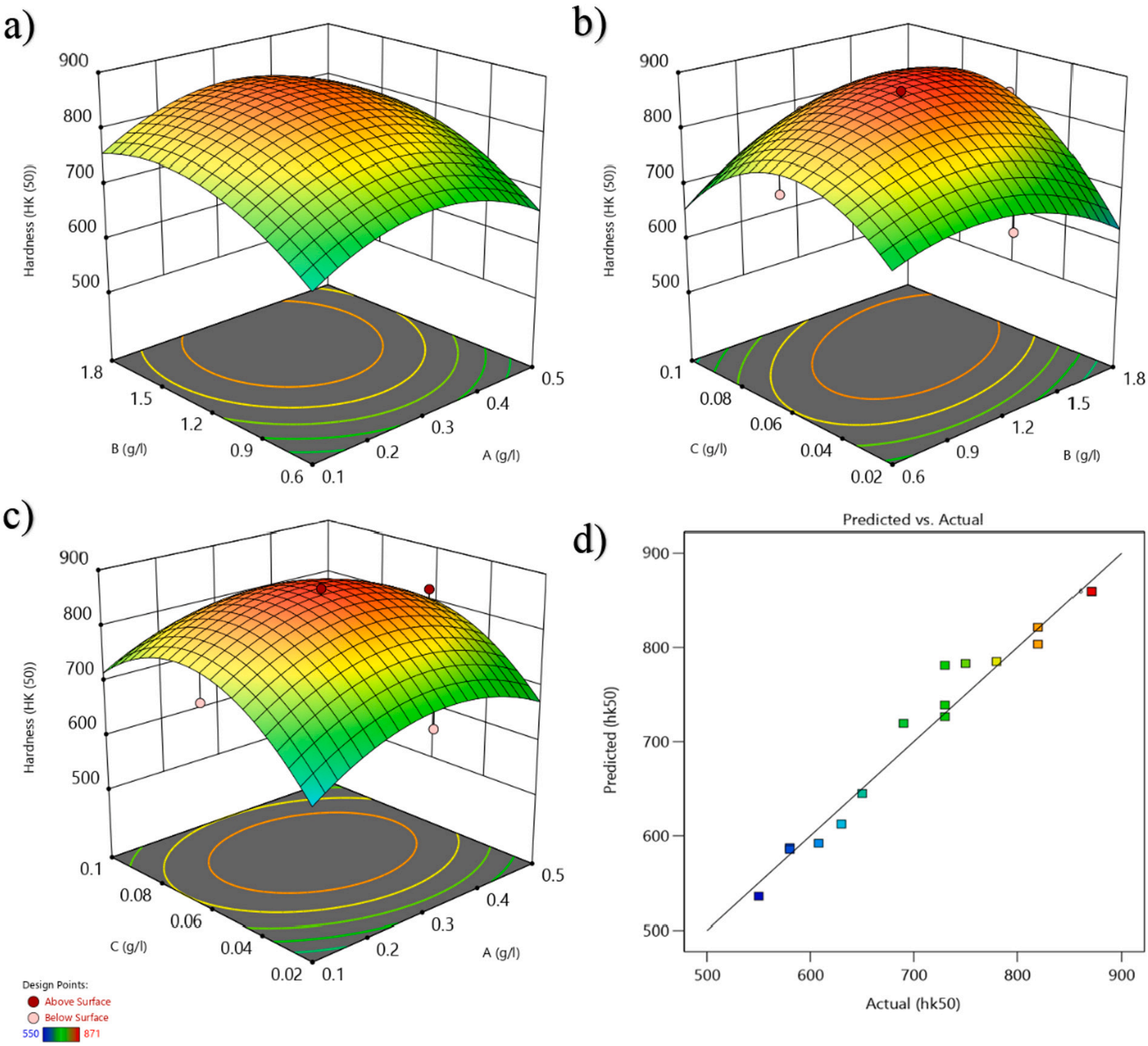

Fig. 4. 3D surface of the effect of a) A and B b) B and C c) A and C variables on the hardness, and d) Plot of the experimental hardness values versus predicted values by RSM.

Table 5

The variable parameters value obtained after the optimization and their predicted responses.

Nanodiamond concentration (g/l)	Reducing agent concentration (g/l)	Stabilizer concentration (g/l)	Predicated hardness value (hk_{50})	Predicated thickness value (μm)	Desirability
0.271	1.624	0.076	852.56	14.26	0.90

3.4. Comparison between optimized Ni-B-nanodiamond and Ni—B coating

3.4.1. Surface morphology and texture of the coating

Fig. 5a and b show the surface morphology of the Ni—B and optimized Ni-B-nanodiamond coatings. As has been mentioned previously by many authors, the texture of coatings consist of cauliflowers with sub-colonies [47,48]. Results show that at the surface of the Ni—B coating the sub-colonies have covered all of the surface, however, the distribution of sub-colonies in the Ni-B-nanodiamond coating is not uniform.

Fig. 5c and d show a backscattered FIB-FESEM image of the Ni—B and optimized Ni-B-nanodiamond coating after polishing. The existence of more dark shadows in Fig. 9b clearly shows nanodiamonds are distributed throughout the coating. The presence of micro-cracks in both samples is due to the formation of internal stress in the coatings during the deposition.

3.4.2. Profile chemistry

The GDOES results of the Ni—B and Ni-B-nanodiamonds coatings are shown in Fig. 6a and b, respectively. In the Ni—B sample boron concentration at the interface is close to 25.3 at. % and it almost remain constant. Fig. 4b shows the carbon content in the Ni-B-nanodiamond coating varied between 6.6 and 4.6 at. %. The boron concentration in Ni-B-nanodiamond is close to 23.9 at. % and it decreases linearly to 18.8 at. % towards the top surface. It is worthy to mention that the thickness of the Ni-B-nanodiamond coating was consistent with 99 % accuracy with the predicted model based on RSM method and 2 μm higher compared to the Ni—B coating.

On the mechanism of Ni-B-nanodiamond deposition it can be said

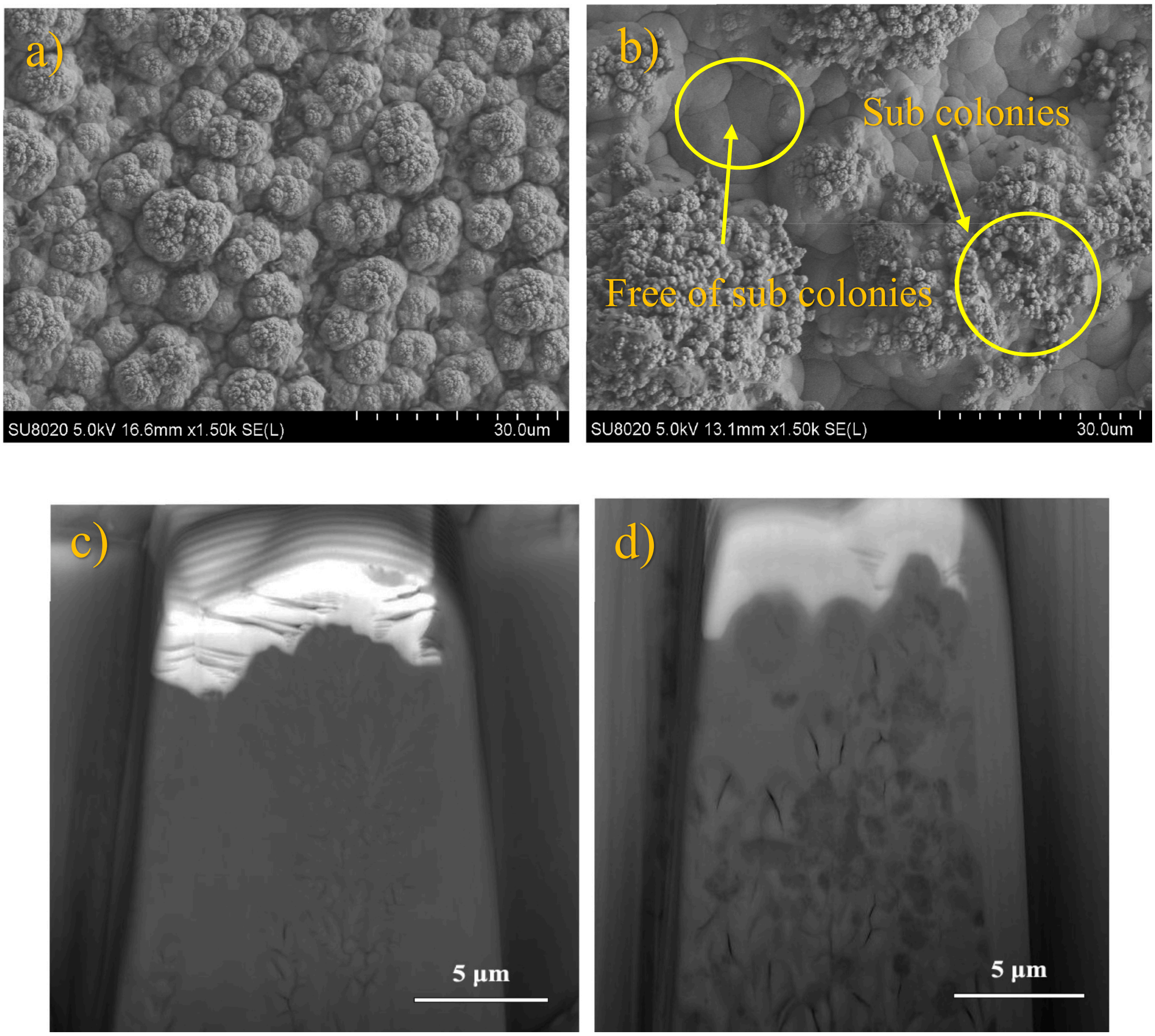

Fig. 5. SEM surface morphology of the a) Ni—B and b) Ni-B-nanodiamonds coating, and FIB-SEM image of the c) Ni—B and d) Ni-B-nanodiamonds coating.

that the Ni^{2+} cations can be reduced at the substrate and nanodiamonds surface [10,45]. Despite the fact that nanodiamonds can act as a reducing agent lower boron content was observed in this sample which is in contrast with their borohydride reduction ability. There is also another factor which can affect the concentration of boron in the coating: it is the adsorption of borohydride ions before the borohydride reduction reaction during the deposition process. To check the effect of the addition of nanodiamonds on the adsorption of borohydride ions, a molecular dynamic simulation was conducted.

3.4.3. *Molecular dynamic simulation of borohydride adsorption during deposition*

The graphical outcomes (side view) generated after the simulation of borohydride adsorption in all systems are visualized in Fig. 7a-c.

The adsorption energy of borohydride for all predefined surfaces is calculated using the following equation [49]:

$$E_{adsorbtion} = E_{total} - (E_{adsorbate+water} + E_{adsorbent+water}) + E_{water} \tag{3}$$

where E_{total} is the total energy of the simulated system; $E_{adsorbate+water}$ and $E_{adsorbent+water}$ are the total energy of adsorbate/water and absorbent/water systems, respectively. E_{water} is the energy of the water system.

The quantitative results of borohydride adsorption energy are summarized in Fig. 7d. All surfaces show the negative value which indicates borohydride can adsorb spontaneously on the three surfaces during deposition. The nanodiamonds show lower adsorption energy compared to the nickel and iron. This might explain why Ni-B-nanodiamond coatings present lower boron content compared to the Ni—B coating. It has been reported by Liu et al. [50]. that the endothermic dehydrogenation reaction of borohydride to produce H+ or H- requires +384 Kcal/mol and + 236 Kcal/mol, energy respectively. Therefore, the calculated adsorption energy of iron and nickel with the values of 286.41 Kcal/mol and 347.23 Kcal/mol indicates that the dehydrogenation reaction of borohydride on the iron and nickel can happen spontaneously to provide the boron atoms for the deposition. However, the nanodiamonds adsorption energy with the value for the 103.56 Kcal/mol is not enough to provide the energy needed for borohydride dehydrogenation.

One of the main reasons for the higher adsorption energy presented by iron and nickel is the fact that the bond lengths for borohydride configuration on Fe and Ni crystal structure hollow site is very close to the bond length of B—H which makes the adsorption easy.

3.4.4. *Hardness and roughness of the coating*

The average value of hardness, elastic modulus, and roughness value of Ni-B-nanodiamond and Ni—B coatings has been shown in Table. 6. Results shows that the microhardness and elastic modulus of the Ni—B has increased by adding nanodiamonds into the electroless bath. The

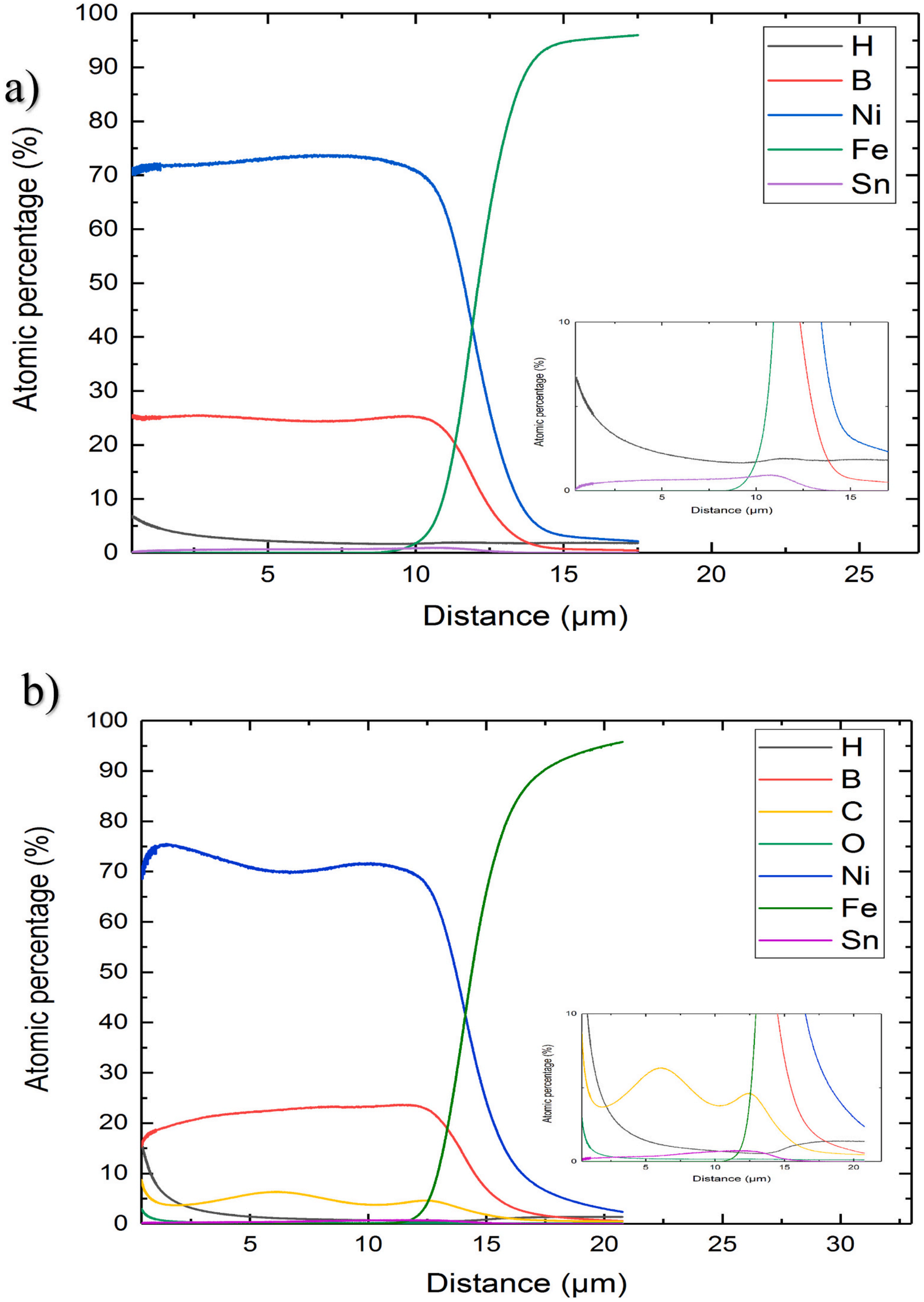

Fig. 6. Depth profile chemical analysis of a) Ni—B and b) Ni-B-nanodiamond coating.

result of microhardness shows 96 % accuracy with our predicted results based on the RSM method. Higher surface roughness value of the Ni-B-nanodiamond coating is due to the non-homogenous structure of sub-colonies which has been described already.

3.4.5. Scratch resistance of the coating

The scratched surface of samples and COF are shown in Fig. 8. The COF increases during the running-in period (Fig. 8a). The increase of the friction coefficient can be categorized into two different stages. At the first stage the friction coefficient is related to the surface hardness and roughness, based on the traditional theories [51,52]. At the second stage, formation of the third layer between coating and diamond stylus due to the higher load value create new contact areas between these two parts which changes the linear slope of the friction diagram. It should be noted that in both stages Ni-B-nanodiamond coating shows the lower COF value. The SEM, EDS and Raman analysis was performed on the marked areas of Fig. 8b.

Fig. 9a, b shows the scratched image of the samples at low load. Local collapsing of the coatings was observed in both coatings, however, severe coating collapse (based on the width of the scratch) along with randomly oriented cracks at the edge of the scratched trace was observed in Ni—B coating. At low loads the surface roughness plays a most prominent role in scratch test. High surface roughness in Ni-B-nanodiamond coating combined effects of tangential and vertical forces on the slip, leading to a wavy interface which created low shear bonds and cracks. [53].

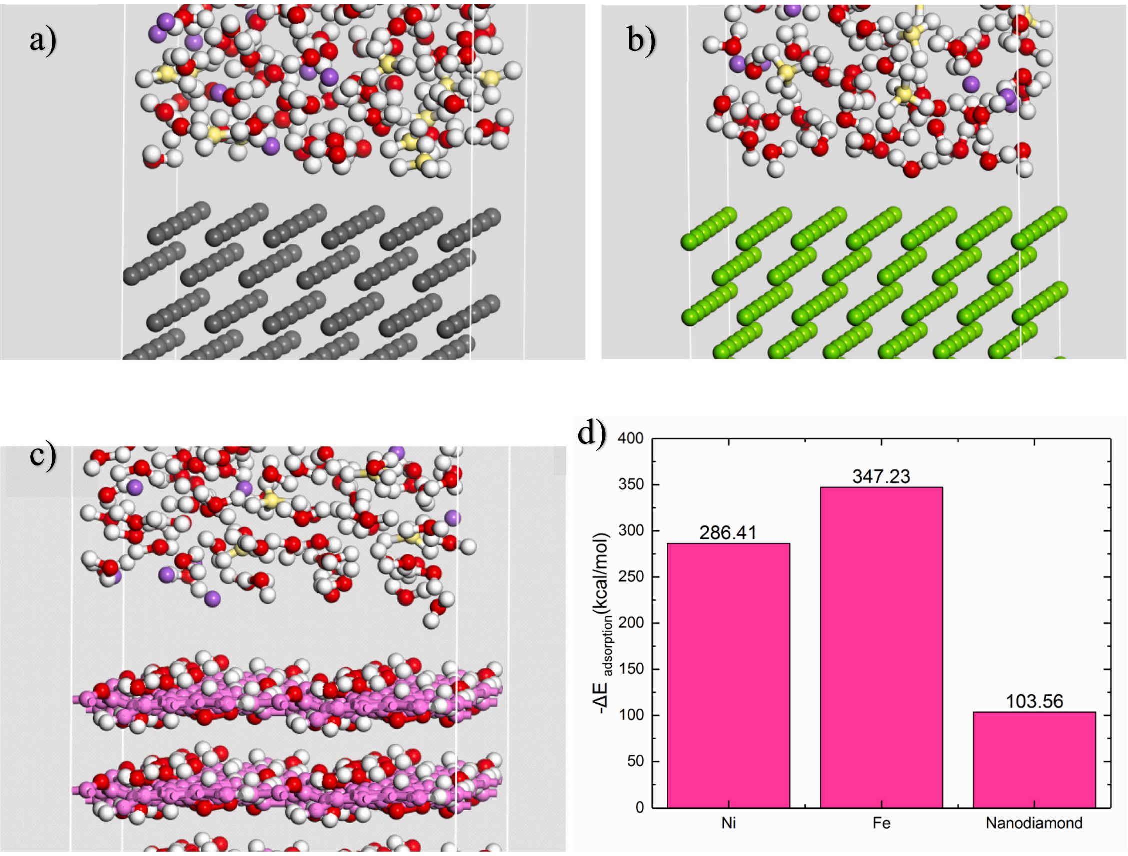

Fig. 7. The inside views of final structures of a) Fe, b) Ni, c) nanodiamond surface in sodium borohydride solution obtained from MD simulation (Fe: grey, Ni: green, hydrogen: white, boron: yellow, carbon: purple, and oxygen red), and d) the computed adsorption energies of the borohydride ions on all surfaces. (For interpretation of the references to colour in this figure legend, the reader is referred to the web version of this article.)

Table 6
Values of the roughness, hardness, and elastic modulus for Ni-B-nanodiamond and Ni—B coating.

Measurements	Ni-B-nanodiamond	Ni-B
Knoop hardness (hk50)	821 ± 23	758 ± 17
Nanoindentation hardness (GPa)	9.29 ± 0.6	9.09 ± 0.3
Elastic modulus (GPa)	165.51 ± 12	149.85 ± 9
Roughness (μm)	1.1 ± 0.09	0.50 ± 0.05

Increasing the load further lead to the formation of semi-circles cracks in both coatings (Fig. 9c and d). Deeper and longer cracks were observed in Ni—B coatings, however, the scratched surface of the Ni-B-nanodiamonds consisted mostly of tiny hairline cracks (Fig. 9e and f). Fig. 9g and h show that at the end of the scratch test there is more coating accumulation and pile up in the Ni—B compared to Ni-B-nanodiamonds coating.

During the scratch test, one tensile stress is formed parallel to the scratch direction and the other perpendicular to the scratch direction. These stresses lead to formation of nano voids near the shear bands and formation of the multi-axial stress [54]. As a result, shear moves preferentially at soften region and off-axial shearing begin. Presence of any cavity, micro-pits or voids in the structure increases the probability of the above theory occurring and lead to formation of long and deep cracks. The presence of hairline cracks in the Ni-B-nanodiamond sample is due to the formation of branch like micro shear bands at the tip of the crack. In fact, when the crack reaches the nanodiamond, many axial shearing will simultaneously form at the shear bands and the crack propagation is blocked (see Fig. S2 in Supporting information).

the Gaussian fitting of Raman spectra of the Ni-B-nanodiamond coating measured on different parts of the scratched surface has been shown in in Supporting information (Fig. S3). The diamond band shows a sharp peak at ~1265 cm^{-1}, and the graphene like carbon structure shows a peak around 1360 and 1550 as the D and G peak respectively. The disordered sp3 carbon also shows a broad peak at 1140 cm^{-1} [55–57].

The deconvolution results are tabulated in Supporting information (Table. S1). At the beginning of the scratch test (with a load up to 48 N) the I_D/I_G and the intensity of the disordered sp3 to diamond increases from 0.93 to 1.82 and 0.34 to 0.49 respectively. Moreover, the FWHM of the diamond band increases from 77.89 to 93.39 cm^{-1}. Results indicate that, at the beginning of the scratch test, diamond grains undergo surface damage, such as micro-cracking and graphitisation. By applying higher load (up to 150 N), the I_D/I_G decreases from 1.82 to 0.72 and the intensity of the disordered sp3 to diamond ratio deceases from 0.49 to 0.43 respectively (Fig. 10a, b). Moreover, the FWHM of the diamond band decreases from 93.39 to 80.54 cm^{-1}. This is due to the fact that by applying higher loads more nanodiamonds will transfer from the Ni—B matrix to the surface. In fact, at this stage, plastic deformation and a shearing-off of metallic material pull out most of nanodiamonds to the surface which makes them act as lubricating material.

The Fe to Ni atomic concentration on each different part of the scratched surface, based on the EDS results, has been shown in Fig. 10c. Results show that the Fe to Ni atomic concentration ratio increased in both coatings at a load of the 48 N, however higher increments of this ratio were observed in the Ni—B coating which indicate more thinning of the Ni—B coating. Interestingly, further increasing the load shows that the Fe to Ni atomic concentration ratio decreases in Ni-B-nanodiamond and increases constantly in the Ni—B coating. This is due to the formation of a third layer in Ni-B-nanodiamond that pulls out

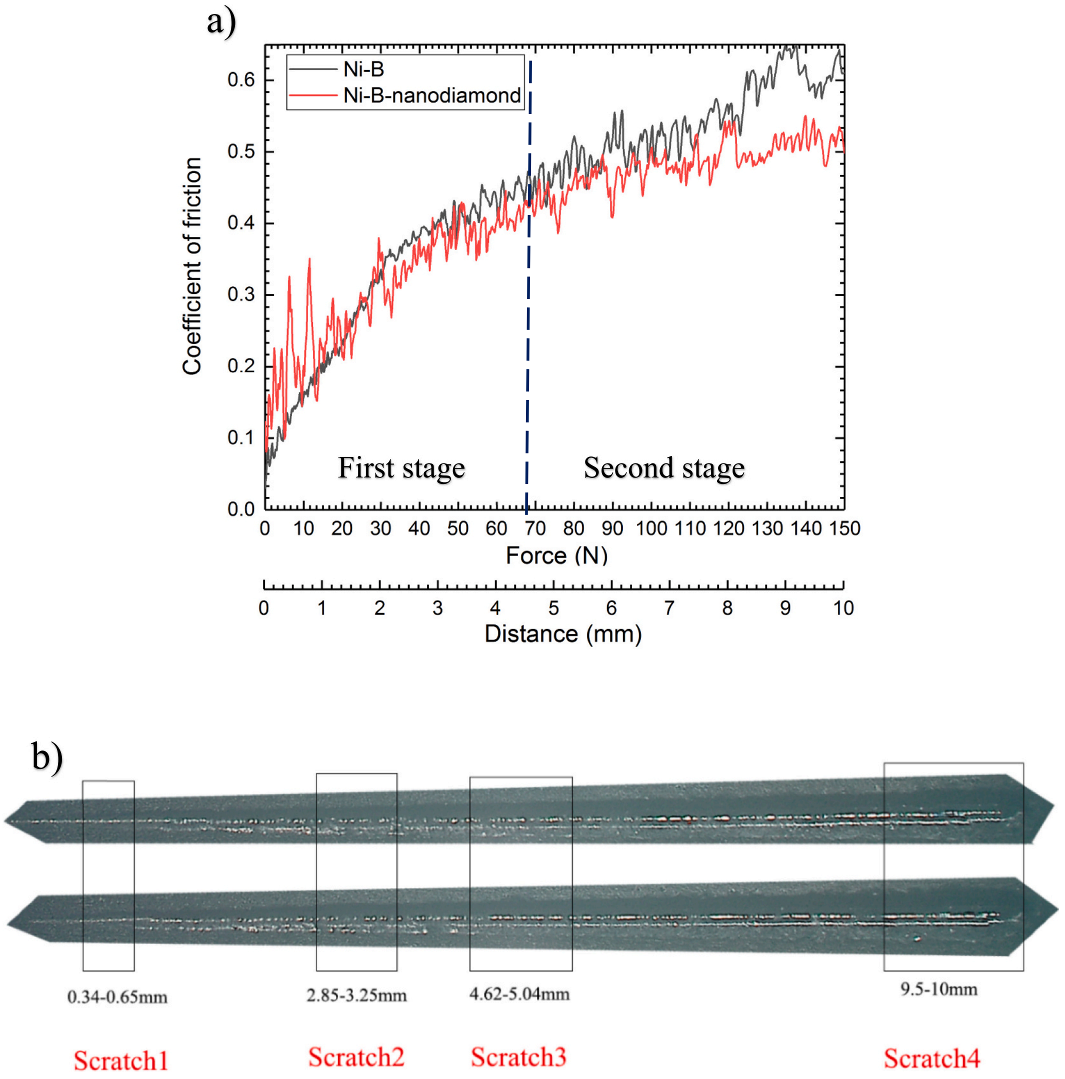

Fig. 8. a) Friction coefficient variations against applied force and distance, b) optical microscopic images of the scratch test with the marked areas for analysis (up: Ni-B-nanodiamond, down: Ni—B).

nanodiamonds to the surface and creates lubrication. Based on the results it can be said that the formed third layer of Ni—B coating could not support the applied load and act as an effective lubricant.

3.4.6. *toughness of the coating*

Fig. 11a and b show the SEM images of the coatings after Rockwell C indentation test. The images show that extreme delamination occurs in the Ni—B coating and cracks are formed in the direction radially from the center of the identifier. Conversely, no evidence of any cracks or delamination was observed in the Ni-B-nanodiamonds coating, which indicates its higher toughness.

According to Griffith theory of fracture, the critical cracking stress for the formation and propagation of a narrow straight crack is depend on young's modulus of materials [58,59]. Results obtained from nanoindentation test previously showed that adding nanodiamond into electroless bath increases the young's modulus which counts as one of the reason for toughness improvement. However, the difference in young's modulus between the 2 coatings is not sufficient to explain this substantial toughness difference. Therefore, to find out the main reason for toughness improvement, Raman spectra measurements and molecular dynamic simulation were conducted to observe the behavior of nanodiamonds during indentation.

The deconvolution results of the Raman spectra of Ni-B-nanodiamond coatings before and after applying the Rockwell C load are shown in Supporting information (Table. S2).

Results showed that, after applying the load, the intensity of the disordered sp3 to diamond ratio increases which indicates damage at the core of the nanodiamonds particle. Interestingly, the I_D/I_G ratio increases less significantly than disordered sp3 to diamond ratio which means that the diamonds undergo more severe damage than graphite. In order to find out the reason for this phenomena molecular dynamic simulation was used to study the change on the interatomic potential of the carbon SP2 and SP3 carbon structure before and after indentation test, and see the possibility of phase transformation (Fig. 12).

When the indenter was placed directly above the SP2 carbon structure, the potential of the carbon domain at the central region of the sample goes towards the value of the -2.5 eV, as a result of a sequence of bond breaking events along the structure [60]. This interatomic potential change of the SP2 carbon structure leads to the formation of strong monatomic carbon chains, which is a common feature of failure of graphene derivatives and metamaterials [61]. These monatomic carbon chains finally break as the indenter moves forward and results in the complete detachment of carbon atoms from the sample. Conversely, results of the simulation for SP3 carbons shows that after indentation test the interatomic potential of the SP3 carbon changes less comparing to the SP3 atoms. The interatomic potential of the SP3 carbons after the

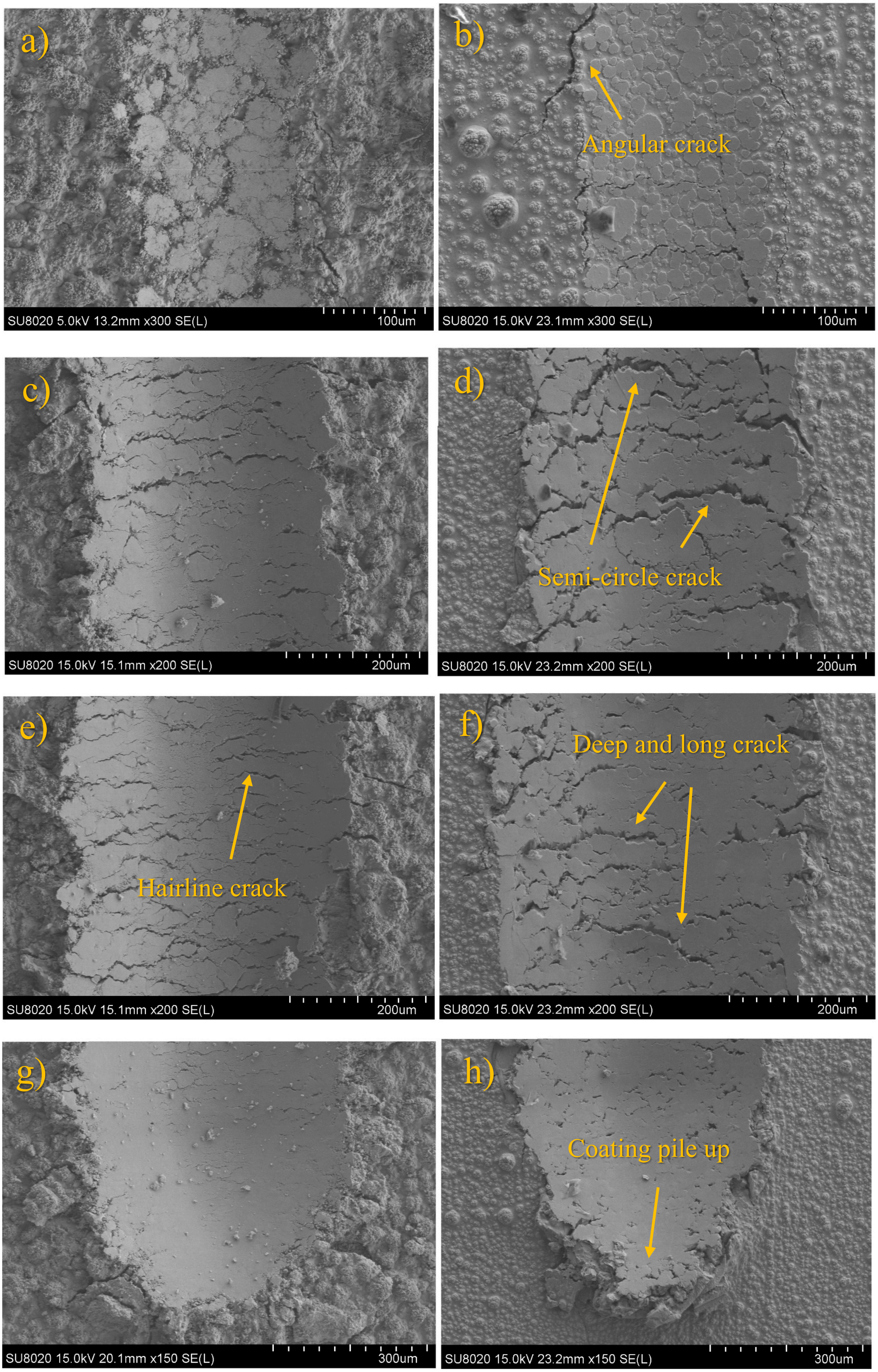

(caption on next page)

Fig. 9. SEM micrographs of scratch 1 of the (a) Ni-B-nanodiamond (b) Ni—B coatings at the load of 5–10 N, scratch 2 of the (c) Ni-B-nanodiamond (d) Ni—B coatings at the load of 42–48 N, scratch 3 of the (e) Ni-B-nanodiamond (f) Ni—B coatings at the load of 68–74 N, scratch 4 of the (g) Ni-B-nanodiamond (h) Ni—B coatings at the load of 140–150 N.

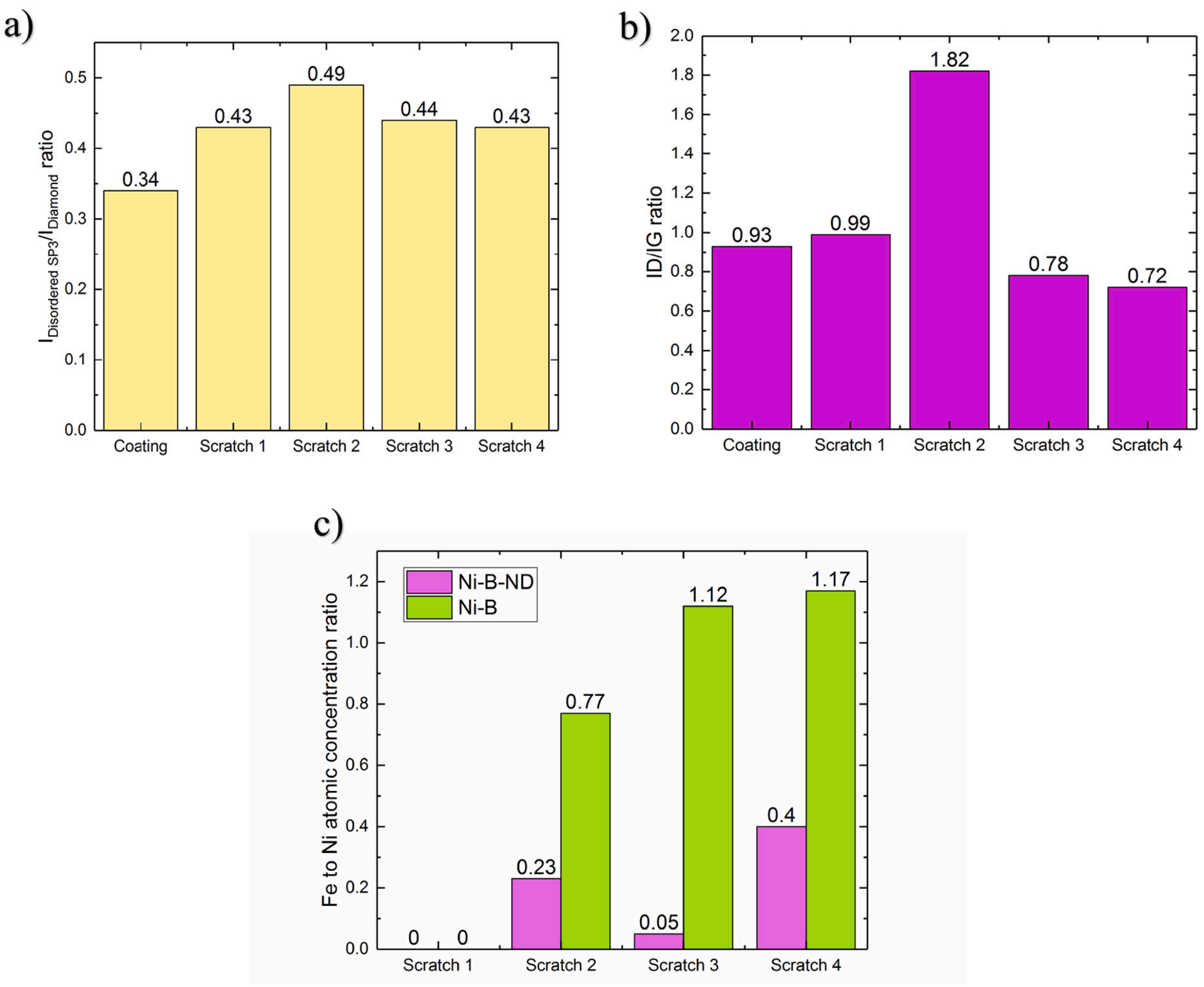

Fig. 10. a) The intensity ratio of the disordered sp3 to diamond, b) the intensity ratio of the D G band, c) the intensity ratio of the Fe to Ni atomic concentration obtained from EDS analysis of different part of scratched surfaces for Ni—B and Ni-B-nanodiamond coating.

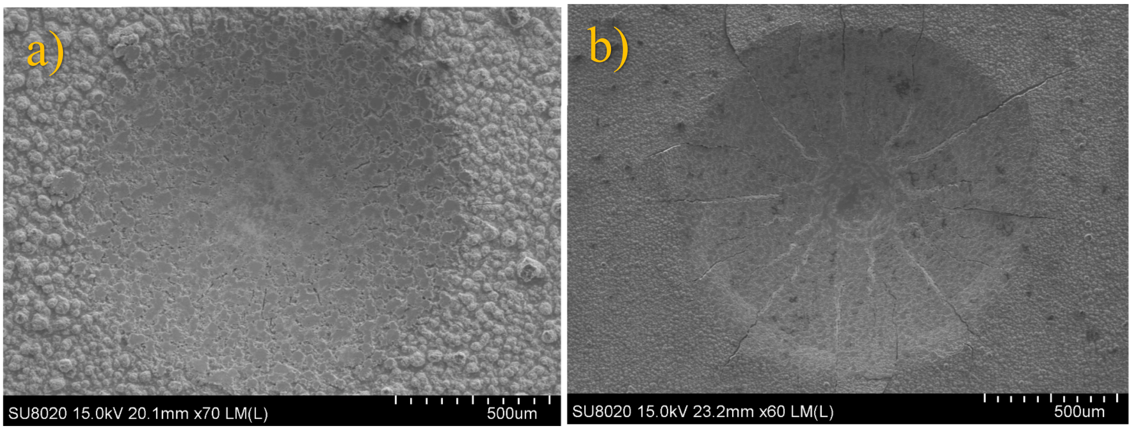

Fig. 11. SEM images of indentations effect on a) Ni-B-nanodiamond and b) Ni—B coating.

indentation was varied between −2.5 and − 8 eV (unlike SP2 carbon layer which all interatomic potential after indentation was close to the −2.5 eV). The lower interatomic potential change of SP3 carbon atoms compared to SP2 carbon atoms means that the SP3 structure is more prone to phase transformation or form a structure with disordered bonds to reach the equilibrium state [62]. In order to verify this hypothesis, the

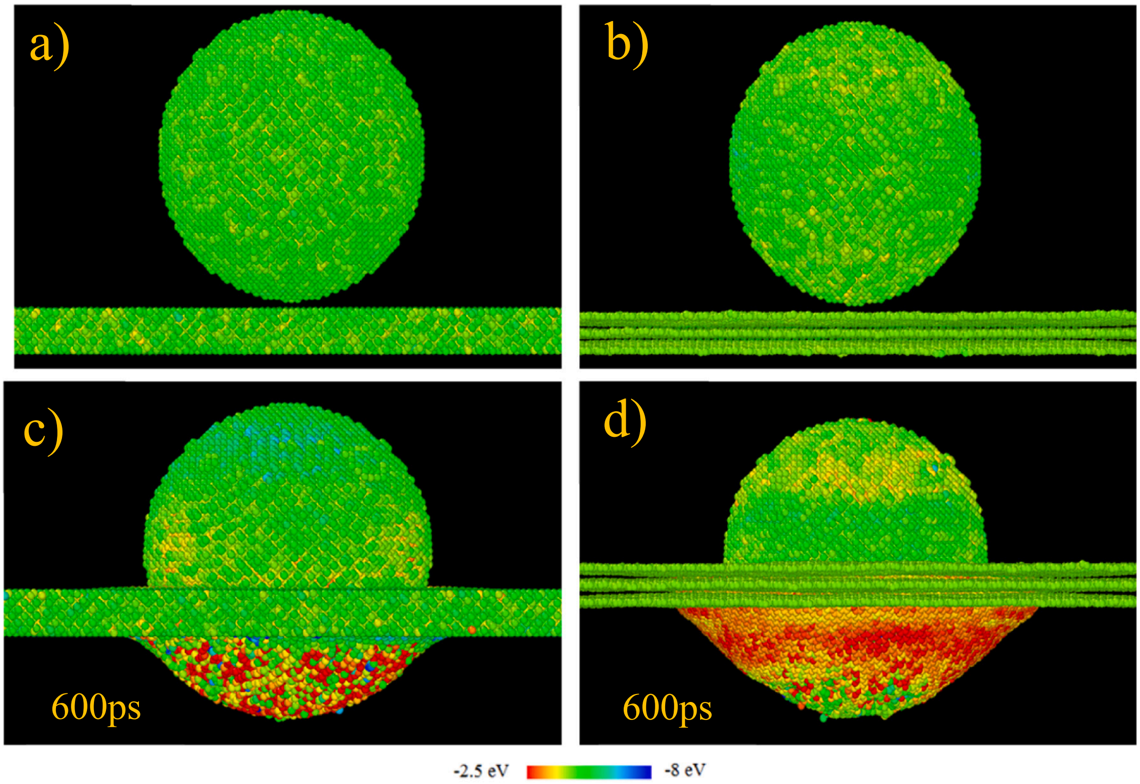

Fig. 12. Change in the interatomic potential of the SP3 carbon layer a) before indentation, c) after indentation, and change in the interatomic potential of the SP2 carbon layer b) before indentation, d) after indentation.

polyhedral template matching (PTM) in Ovito program was applied [63] to monitor SP3 phase transformation during the indentation process. The results of the polyhedral template matching during the simulation identifies two crystallographic phases namely diamond cubic and graphite HCP phases by calculating the interatomic distances between carbon atoms. Results of the simulation indicates that as the indenter proceeds more and more SP3 carbon is transformed to the graphite structure (see Fig. S4 in Supporting information), and at the end of the

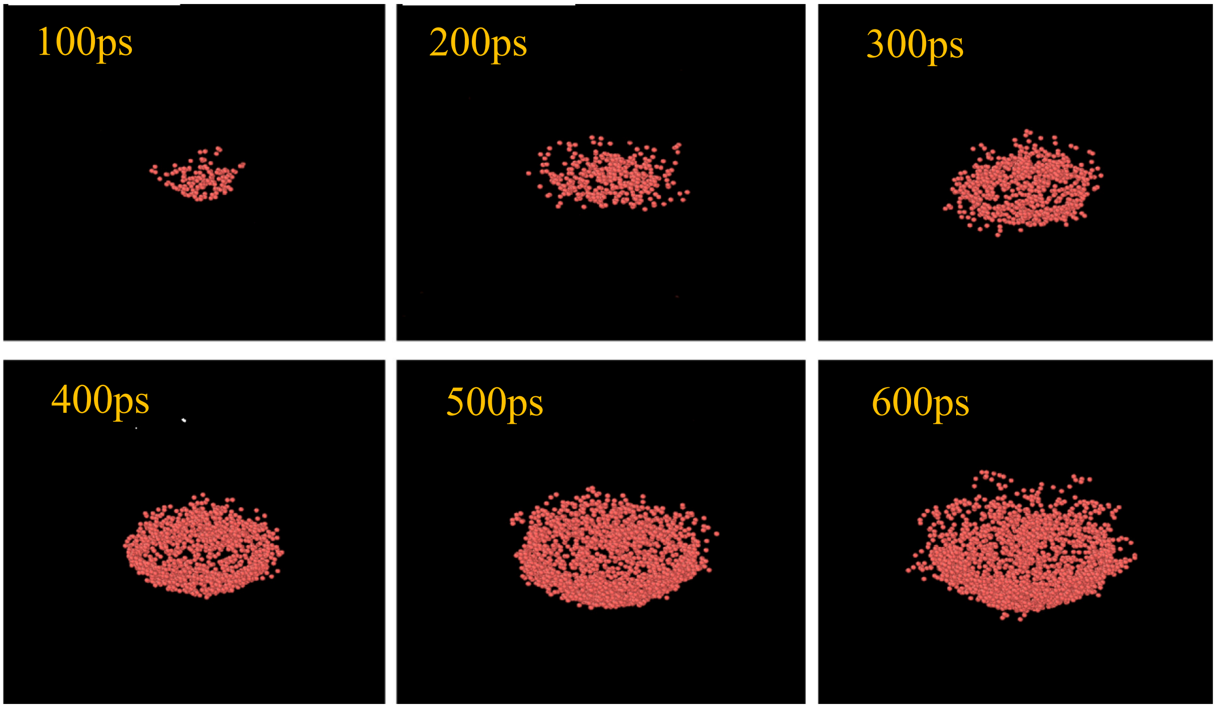

Fig. 13. Polyhedral template matching results from Ovito showing the HCP graphite carbons form due to the SP3 carbon phase transformation during indentation test at the surface of diamond.

simulation 12.23 % SP3 carbon atoms transfer from SP3 diamond cubic to graphite HCP phase (SP2 atoms).

Fig. 13 shows the number of SP3 diamond carbon structure transformed to graphite HCP carbon structure during the indentation. Transformation of the diamond to graphite might starts from diamond's (111), (110), and (100) plane. However, among all of them it is assumed that due to the similarity between the structure of the graphite plane and (111) diamond plane this atomic rearrangement requires less energy than the diamond graphitization from the others. That might explain why not all of the atoms on diamond transformed to graphite during indentation.

Based on the simulation results it can be concluded that the reason for small change of the I_D/I_G ratio comparing to diamond to disordered SP3 ratio after the indentation test is the fact that SP3 atoms undergoes phase transformation and more graphite are formed at the surface.

This phase transformation is the reason for higher toughness of the Ni-B-nanodiamond coating compared to the Ni—B coating. Due to the fact that diamond to graphite transformation induces volume expansion and produce a compressive stress field around the crack to inhibit and stop it propagation during indentation. On the other hand, the volume expansion energy can reduce the stress concentration around the crack tip region. As a result of preventing the crack formation the mechanical behavior of the coating will not reduce during indentation and coating shows high toughness behavior.

4. Conclusion

In this research, after improving the nanodiamonds stability through functionalization, the hardness and deposition rate of the electroless Ni-B-nanodiamond coating were optimized by varying the nanodiamond, reducing agent, and stabilizer concentration in electroless bath using the RSM method. The following conclusions can be drawn from the research work:

- Functionalization of nanodiamonds in HNO_3/H_2SO_4 (1:3 V/V) solution prevents nanodiamonds agglomeration in alkaline solution (pH 14). However, the SP3 to SP2 ratio decreases from 2.96 to 1.66.
- Quadratic models were developed for the optimization of bath parameters to achieve the highest hardness and deposition rate based on RSM method and the models were found to be mathematically appropriate for optimization. Analysis of variance (ANOVA) revealed that the stabilizer concentration has the maximal influence on composite coating deposition rate and hardness.
- Despite the fact that it has been proven by other researchers that nanodiamonds, as carbon allotropes, can act as a reducing agent, our molecular dynamic simulation results showed that the low adsorption energy of borohydride on nanodiamonds surface is not sufficient for borohydride dehydrogenation and decreases the reduction reaction rate. GDOES results on the coating surface verify the validity of the simulation by measuring the boron content of the coating.
- Raman spectra results on the scratched surface of coating showed that at lower scratch force nanodiamonds undergo micro-cracking and graphitization which block cracks propagation, and at higher loads the lubricating effect of the third layer formed between the coating and stylus improves due to the presence of nanodiamonds.
- The Raman spectroscopy on the Rockwell c indentation test sites showed that the core of the nanodiamonds undergoes more damage than the SP2 carbons which surrounded diamond core. However, molecular dynamic simulation results showed that this is due to the fact that 12.23 % of SP3 carbon atoms transfer from diamond cubic to graphite HCP phase as the indenter proceeds on diamonds surface and as a result the amount of SP2 carbon increases.

Since, only a handful of studies have studied the mechanism of ND adhesion improvement in composite coating using MD simulation and Raman spectroscopy, and also as role ND of in deposition of electroless Ni—B is not investigated the present investigation could pave the way to further research.

CRediT authorship contribution statement

Sepehr Yazdani: Conceptualization, Investigation, Methodology, Software, Validation, Writing – original draft. **Veronique Vitry:** Conceptualization, Supervision, Writing – review & editing, Validation.

Declaration of competing interest

The authors declare that they have no known competing financial interests or personal relationships that could have appeared to influence the work reported in this paper.

Data availability

No data was used for the research described in the article.

Acknowledgements

One of the authors (Sepehr Yazdani) wishes to thank Belgian National Fund for Scientific Research (FNRS) for the financial support in the framework of the Aspirant project. The authors also want to thank to Mr. Yoann Paint at Belgium Materia Nova Research Centre for the SEM analysis, Mr. Patrick Chapon at HORIBA France SAS for GDOES analysis, and Mr. Vedi Dupont at Belgian Ceramic Research Centre for FIB analysis.

Appendix A. Supplementary data

Supplementary data to this article can be found online at https://doi.org/10.1016/j.surfcoat.2022.129133.

References

[1] V. Vitry, J. Hastir, A. Mégret, S. Yazdani, M. Yunacti, L. Bonin, Recent advances in electroless nickel-boron coatings, Surf. Coat. Technol. 429 (2022), 127937.

[2] H. Algul, M. Uysal, A. Alp, A comparative study on morphological, mechanical and tribological properties of electroless NiP, NiB and NiBP coatings, Appl. Surf. Sci. Adv. 4 (2021), 100089.

[3] D. Erhan, F. Doğan, M. Uysal, H. Akbulut, S. Aslan, Optimization of Ni-B coating bath and effect of DMAB concentration on hardness and wear, Surf. Interfaces 22 (2021), 100880.

[4] M. Sundararajan, M. Devarajan, M. Jaafar, Electroless Ni–B sealing on nanoporous anodic aluminum oxide pattern: deposition and evaluation of its characteristic properties, J. Mater. Res. Technol. 19 (2022) 4504–4516.

[5] E. Correa, A.A.Z. Gil, J.G. Castaño, F. Echeverría, Activation, initiation, and growth of electroless nickel coatings, in: Electroless Nickel Plating, CRC Press, 2019, pp. 31–86.

[6] J.K. Pancrecious, S.B. Ulaeto, R. Ramya, T.P.D. Rajan, B.C. Pai, Metallic composite coatings by electroless technique–a critical review, Int. Mater. Rev. 63 (8) (2018) 488–512.

[7] A. Tozar, İ.H. Karahan, Effect of octylphenyl ether group nonionic surfactant on the electrodepositon of the hexagonal boron nitride reinforced ni-B matrix composite coatings, Surf. Coat. Technol. 381 (2020), https://doi.org/10.1016/j.surfcoat.2019.125131.

[8] Q. Barati, S.M.M. Hadavi, Electroless ni-B and composite coatings: a critical review on formation mechanism, properties, applications and future trends, Surf. Interfaces 21 (2020), 100702, https://doi.org/10.1016/j.surfin.2020.100702.

[9] J.K. Pancrecious, J.P. Deepa, V. Jayan, U.S. Bill, T.P.D. Rajan, B.C. Pai, Nanoceria induced grain refinement in electroless ni-B-CeO2 composite coating for enhanced wear and corrosion resistance of aluminium alloy, Surf. Coat. Technol. 356 (2018) 29–37.

[10] S. Yazdani, R. Tima, F. Mahboubi, Investigation of wear behavior of as-plated and plasma-nitrided ni-B-CNT electroless having different CNTs concentration, Appl. Surf. Sci. 457 (2018) 942–955.

[11] S. Sürdem, C. Eseroğlu, R. Çitak, A parametric study on the relationship between NaBH4 and tribological properties in the nickel-boron electroless depositions, Mater. Res. Express 6 (12) (2019), 125085.

[12] S.A. Abdel-Gawad, M.A. Sadik, M.A. Shoeib, Preparation and properties of a novel nano ni-B-sn by electroless deposition on 7075–T6 aluminum alloy for aerospace application, J. Alloys Compd. 785 (2019) 1284–1292.

[13] R. Tima, F. Mahboubi, Ability of plasma nitriding to improve tribological behavior of medium and high boron electroless nickel coatings, Tribol. Int. 156 (2021), 106822.
[14] E. Georgiza, V. Gouda, P. Vassiliou, Production and properties of composite electroless ni-B-SiC coatings, Surf. Coat. Technol. 325 (2017) 46–51.
[15] C. Ma, D. Zhao, W. Liu, F. Xia, P. Jin, C. Sun, Magnetic assisted pulse electrodeposition and characterization of Ni–TiC nanocomposites, Ceram. Int. 46 (11) (2020) 17631–17639.
[16] C. Liu, Y. Yin, C. Li, M. Xu, R. Li, Q. Chen, Preparation and properties of ni-P/Bi self-lubricating composite coating on copper alloys, Surf. Coat. Technol. 443 (2022), 128617.
[17] P. Murali, R. Gopi, I. Saravanan, A. Devaraju, M. Karthikeyan, Wear and mechanical properties of electroless NiP and NiP-Silicon Carbide (SiC) composite coatings on En8 steel, Mater. Today: Proc. 68 (2022) 1707–1710.
[18] Y. Zhang, K.Y. Rhee, D. Hui, S.-J. Park, A critical review of nanodiamond based nanocomposites: synthesis, properties and applications, Compos. Part B 143 (2018) 19–27.
[19] F. Zhang, T. Liu, Nanodiamonds reinforced titanium matrix nanocomposites with network architecture, Compos. Part B 165 (2019) 143–154.
[20] H. Matsubara, G. Kikugawa, T. Bessho, T. Ohara, Evaluation of thermal conductivity and its structural dependence of a single nanodiamond using molecular dynamics simulation, Diam. Relat. Mater. 102 (2020), 107669.
[21] L. Reinert, M. Zeiger, S. Suárez, V. Presser, F. Mücklich, Dispersion analysis of carbon nanotubes, carbon onions, and nanodiamonds for their application as reinforcement phase in nickel metal matrix composites, RSC Adv. 5 (115) (2015) 95149–95159.
[22] V. Mochalin, O. Shenderova, D. Ho, Y. Gogotsi, The properties and applications of nanodiamonds, Nano-Enabled Med. Appl. (2020) 313–350.
[23] Y. Zamani, et al., Nanodiamond-containing composites for tissue scaffolds and surgical implants: a review, J. Compos. Compd. 2 (5) (2020) 215–227.
[24] H. Aghamohammadi, A. Heidarpour, R. Jamshidi, O. Bayat, Tribological behavior of epoxy composites filled with nanodiamond and Ti3AlC2TiC particles: a comparative study, Ceram. Int. 45 (7) (2019) 9106–9113.
[25] Y. Zhang, J.R. Choi, S.-J. Park, Thermal conductivity and thermo-physical properties of nanodiamond-attached exfoliated hexagonal boron nitride/epoxy nanocomposites for microelectronics, Compos. A: Appl. Sci. Manuf. 101 (2017) 227–236.
[26] W. Zhang, et al., Stable li-metal deposition via a 3D nanodiamond matrix with ultrahigh young's modulus, Small Methods 3 (11) (2019) 1900325.
[27] S.S. Mirhosseini, F. Mahboubi, Effect of plasma nitriding on tribological properties of nickel-boron-nanodiamond electroless coatings, Surf. Coat. Technol. 435 (2022), 128216.
[28] I. Makarova, et al., Nickel-nanodiamond coatings electrodeposited from tartrate electrolyte at ambient temperature, Surf. Coat. Technol. 380 (2019), 125063.
[29] M. Liu, et al., Effect of nanodiamond concentration and the current density of the electrolyte on the texture and mechanical properties of Ni/nanodiamond composite coatings produced by electrodeposition, Materials 12 (7) (2019) 1105.
[30] D. Wang, F. Li, M. Liu, W. Zhang, X. Yu, W. Da, Effect of nanodiamond content in the plating solution on the corrosion resistance of nickel-nanodiamond composite coatings prepared on annealed 45 carbon steel, Coatings 12 (10) (2022) 1558.
[31] K. Xie, et al., Surface functionalization of nanodiamonds and simultaneous enhancement to the strength and ductility of nanodiamond/2024Al composites, Mater. Sci. Eng. A 844 (2022), 143200.
[32] H. Ma, et al., Influence of nano-diamond content on the microstructure, mechanical and thermal properties of the ZK60 composites, J. Magnes. Alloys 10 (2) (2022) 440–448.
[33] M.G. Chernysheva, A.G. Popov, V.N. Tashlitsky, G.A. Badun, Cationic surfactant coating nanodiamonds: adsorption and peculiarities, Colloids Surf. A Physicochem. Eng. Asp. 565 (2019) 25–29.
[34] O.R. Monteiro, S. Murugesan, V. Khabashesku, Electroplated Ni–B films and Ni–B metal matrix diamond nanocomposite coatings, Surf. Coat. Technol. 272 (2015) 291–297.
[35] E. Ōsawa, D. Ho, H. Huang, M.V. Korobov, N.N. Rozhkova, Consequences of strong and diverse electrostatic potential fields on the surface of detonation nanodiamond particles, Diam. Relat. Mater. 18 (5–8) (2009) 904–909.
[36] S.A. El-Demrdash, et al., The effect of salt and particle concentration on the dynamic self-assembly of detonation nanodiamonds in water, Nanoscale 13 (33) (2021) 14110–14118.
[37] A.S. Barnard, Self-assembly in nanodiamond agglutinates, J. Mater. Chem. 18 (34) (2008) 4038–4041.
[38] Z. Razaghi, M. Rezaei, Corrosion mechanism of sulfate, chloride, and tetrafluoroborate ions interacted with ni-19 wt% cr coating: a combined experimental study and molecular dynamics simulation, J. Mol. Liq. 319 (2020), 114243.
[39] S.J. Stuart, A.B. Tutein, J.A. Harrison, A reactive potential for hydrocarbons with intermolecular interactions, J. Chem. Phys. 112 (14) (2000) 6472–6486.
[40] R. Mirzaamiri, S. Akbarzadeh, S. Ziaei-Rad, D.-G. Shin, D.-E. Kim, Molecular dynamics simulation and experimental investigation of tribological behavior of nanodiamonds in aqueous suspensions, Tribol. Int. 156 (2021), 106838.
[41] F. Zhao, et al., Graphene-nanodiamond heterostructures and their application to high current devices, Sci. Rep. 5 (1) (2015) 1–11.
[42] F.Y. Xie, et al., Surface characterization on graphitization of nanodiamond powder annealed in nitrogen ambient, Surf. Interface Anal. 42 (9) (2010) 1514–1518.
[43] J. Guo, et al., Crown ethers in graphene, Nat. Commun. 5 (1) (2014) 1–6.
[44] P. Liu, B. Hao, H. Zhang, B. Xu, J. Guo, Atomic-scale investigation of carbon-based materials by gentle transmission electron microscopy, New Carbon Mater. 36 (3) (2021) 497–511.
[45] S. Yazdani, F. Mahboubi, R. Tima, O. Sharifahmadian, Effect of carbon nanotube concentration on the corrosion behavior of electroless ni-B-CNT coating, J. Mater. Eng. Perform. 28 (6) (2019) 3446–3459.
[46] M.A. Montes-Morán, D. Suárez, J.A. Menéndez, E. Fuente, On the nature of basic sites on carbon surfaces: an overview, Carbon 42 (7) (2004) 1219–1225.
[47] K. Krishnaveni, T.S.N.S. Narayanan, S.K. Seshadri, Electroless Ni–B coatings: preparation and evaluation of hardness and wear resistance, Surf. Coat. Technol. 190 (1) (2005) 115–121.
[48] S. Yazdani, F. Mahboubi, Comparison between microstructure, wear behavior, and corrosion resistance of plasma-nitrided and vacuum heat-treated electroless Ni–B coating, J. Bio- Tribo-Corros. 5 (3) (2019) 1–11.
[49] X. Liu, et al., Adsorption of ammonia nitrogen and phenol onto the lignite surface: an experimental and molecular dynamics simulation study, J. Hazard. Mater. 416 (2021), 125966.
[50] B. Liu, et al., Insight into catalytic mechanisms for the reduction of nitrophenol via heterojunctions of gold nanoclusters on 2D boron nitride nanosheets, ChemNanoMat 5 (6) (2019) 784–791.
[51] A. Matthews, S. Franklin, K. Holmberg, Tribological coatings: contact mechanisms and selection, J. Phys. D. Appl. Phys. 40 (18) (2007) 5463.
[52] K. Holmberg, A. Matthews, Coatings Tribology: Properties, Mechanisms, Techniques and Applications in Surface Engineering, Elsevier, 2009.
[53] S.J. Bull, E.G. Berasetegui, An overview of the potential of quantitative coating adhesion measurement by scratch testing, Tribol. Int. 39 (2) (2006) 99–114.
[54] N.X. Randall, The current state-of-the-art in scratch testing of coated systems, Surf. Coat. Technol. 380 (2019), 125092.
[55] V.I. Korepanov, et al., Carbon structure in nanodiamonds elucidated from raman spectroscopy, Carbon 121 (2017) 322–329.
[56] E.J. Ekoi, D.P. Dowling, Evaluation of the microstructure, mechanical and tribological properties of nickel-diamond nanocomposite coatings, Diam. Relat. Mater. 94 (2019) 118–128.
[57] K.-W. Sun, J.Y. Wang, T.Y. Ko, Raman spectroscopy of single nanodiamond: phonon-confinement effects, Appl. Phys. Lett. 92 (15) (2008), 153115.
[58] W. Zhou, Z. Zhang, N. Li, W. Yan, Y. Li, G. Ye, The preparation of mullite foamed ceramics reinforced by in-situ SiC whiskers and their reinforcement mechanism, Ceram. Int. 48 (10) (2022) 14224–14230.
[59] L. Li, J. Fan, J. Tian, H. Cheng, H. Zhang, Modification of the interface and its influence on the performance of W-6 wt% TiC composite, Mater. Sci. Eng. A 819 (2021), 141442.
[60] G.M. Galiullina, N.D. Orekhov, V.V. Stegailov, Nucleation of carbon nanostructures: molecular dynamics with reactive potentials, J. Phys. Conf. Ser. 774 (1) (2016) 12033.
[61] D. Maroudas, A.R. Muniz, A. Ramasubramaniam, Structure-properties relations in graphene derivatives and metamaterials obtained by atomic-scale modeling, Mol. Simul. 45 (14–15) (2019) 1173–1202.
[62] L. Bai, P.-P. Sun, B. Liu, Z. Liu, K. Zhou, Mechanical behaviors of T-carbon: a molecular dynamics study, Carbon 138 (2018) 357–362.
[63] P.M. Larsen, S. Schmidt, J. Schiøtz, Robust structural identification via polyhedral template matching, Model. Simul. Mater. Sci. Eng. 24 (5) (2016) 55007.